

Magnetic, thermal, and topographic imaging with a nanometer-scale SQUID-on-cantilever scanning probe

M. Wyss,^{1,2} K. Bagani,¹ D. Jetter,¹ E. Marchiori,¹ A. Vervelaki,¹
B. Gross,¹ J. Ridderbos,¹ S. Gliga,³ C. Schönenberger,^{1,2} and M. Poggio^{1,2}

¹*Department of Physics, University of Basel, 4056 Basel, Switzerland*

²*Swiss Nanoscience Institute, University of Basel, 4056 Basel, Switzerland*

³*Swiss Light Source, Paul Scherrer Institute, 5232 Villigen, Switzerland*

(Dated: September 15, 2021)

Abstract

Scanning superconducting quantum interference device (SQUID) microscopy is a magnetic imaging technique combining high field sensitivity with nanometer-scale spatial resolution. State-of-the-art SQUID-on-tip probes^{1,2} are now playing an important role in mapping correlation phenomena, such as superconductivity³ and magnetism⁴, which have recently been observed in two-dimensional van der Waals materials. Here, we demonstrate a scanning probe that combines the magnetic and thermal imaging provided by an on-tip SQUID with the tip-sample distance control and topographic contrast of a non-contact atomic force microscope (AFM). We pattern the nanometer-scale SQUID, including its weak-link Josephson junctions, via focused ion beam milling at the apex of a cantilever coated with Nb, yielding a sensor with an effective diameter of 365 nm, field sensitivity of $9.5 \text{ nT}/\sqrt{\text{Hz}}$ and thermal sensitivity of $620 \text{ nK}/\sqrt{\text{Hz}}$, operating in magnetic fields up to 1.0 T. The resulting SQUID-on-lever is a robust AFM-like scanning probe that expands the reach of sensitive nanometer-scale magnetic and thermal imaging beyond what is currently possible.

Nanometer-scale magnetic imaging techniques, based on optical, electron, x-ray, or scanning probe sensors, reveal magnetization patterns, spin configurations, and current distributions. They provide local information about length-scales, inhomogeneity, and interactions, that is inaccessible in bulk measurements of transport, magnetization, susceptibility, or heat capacity. In recent years, these techniques have shed light on nanometer-scale phenomena such as domain walls, magnetic and superconducting vortices, and magnetic skyrmions. The techniques combining the highest sensitivity and highest spatial resolution are being used to map recently discovered correlated states hosted in some two-dimensional (2D) van der Waals materials and their heterostructures, because they can provide information on quantum phases, including on the spatial variation of order parameters, the presence of domains, and the role of defects. Correlated states in 2D materials are extremely sensitive to disorder and inhomogeneity. In such a fragile environment, local measurements – with sensors whose characteristic size is smaller than the length scale of the disorder – are essential for making sense of the system.

Foremost among sensitive and high-resolution magnetic imaging techniques is scanning superconducting quantum interference device (SQUID) microscopy with so-called SQUID-on-tip probes^{1,2}. These probes consist of a SQUID fabricated by shadow evaporation or directional sputtering of a metallic superconductor directly on the end of a pulled quartz tip. The resulting sensors can have diameters as small as 50 nm and sensitivities down to $5 \text{ nT}/\sqrt{\text{Hz}}$ ⁵. Scanning SQUID-on-tip probes have been used to image superconducting vortices^{6,7}, superparamagnetism at the nanometer-scale^{8,9}, and magnetic reversal in nanomagnetic structures^{10,11}. In 2D systems, they have been used to visualize quantum Hall edge currents in graphene¹² as well as twist-angle disorder³ and orbital magnetism⁴ in twisted bilayer graphene. They have also been used for thermal sensing, achieving sensitivities better than $0.5 \text{ } \mu\text{K}/\sqrt{\text{Hz}}$ ¹³. Such sensitive thermal microscopy, which was recently used to visualize dissipation in the quantum Hall state in graphene¹⁴, is possible only because of its on-tip geometry, allowing the SQUID sensor to be in close proximity to the sample, rather than a pick-up loop, inductively coupled to a distant on-chip SQUID. However, SQUID-on-tip probes, which are typically coupled to stiff tuning fork resonators for stabilization of the tip-sample distance, are only sensitive to topography within tens of nanometers of the surface. Their intrinsic stiffness makes stabilization and topographic imaging challenging and results in a high probability of the tip crashing.

Here, we use focused ion beam (FIB) milling to fabricate a nanometer-scale SQUID at the apex of a cantilever force sensor, combining the capabilities of a SQUID-on-tip with those of non-contact atomic force microscopy (AFM). All components of the SQUID, including superconducting leads, loop, and weak-link Josephson junctions are patterned via direct FIB milling of a sputtered Nb film, overcoming the challenge of patterning directly on a high-aspect-ratio tip. The result is a SQUID-on-lever scanning probe that provides exquisite magnetic, thermal, and topographic contrast. The non-contact AFM cantilever platform provides excellent control of the tip-sample spacing, as well as topographic contrast further than $1\ \mu\text{m}$. In addition, FIB patterning offers flexibility in the possible designs of the SQUID. In contrast, the minimum size and complexity of SQUID-on-tip probes are restricted by the fabrication process, e.g. not allowing for the integration of field coils for susceptibility measurements or flux feedback.

The fabrication of a SQUID at the apex of a commercially available Si-cantilever designed for non-contact AFM is presented schematically in Fig. 1 (a). We use a Ga^+ FIB to mill away the tip of the cantilever, leaving a triangular plateau, on which the SQUID is to be patterned. As part of this process, a small protrusion is left on the side of the plateau, as seen on the right side of the scanning electron microscope (SEM) image in Fig. 1 (c). The role of this feature is both to act as a sharp tip to optimize spatial resolution in AFM mode and to prevent the SQUID from touching the sample surface during scanning. After this first milling step, we deposit a thin film of Nb on the front side of the cantilever. We then pattern the SQUID on the coated cantilever via direct milling of the Nb film with a Ga^+ FIB. This process entails first cutting a long trench in the film through the middle of the cantilever, from its base up to its triangular plateau. The SEM image in Fig. 1 (b) shows the FIB-cut trench which defines two electrical contacts running from the base of the cantilever to its apex. We then mill a hole in the center of the triangular plateau followed by a second, shorter trench. Both the long and short trenches are separated by the central hole and together define two narrow constrictions forming Dayem bridge Josephson junctions (JJs) and hence a Nb SQUID at the tip of the cantilever. Fig. 1 (c) shows the SQUID with loop diameter of 300 nm and a protruding tip of height 175 nm. Finally, a thin film of Pt is patterned via FIB-induced deposition to serve as a shunt resistor between the two Nb leads, as shown in Fig. 1 (d).

The resulting SQUID-on-lever is mounted in a custom-built scanning probe microscope

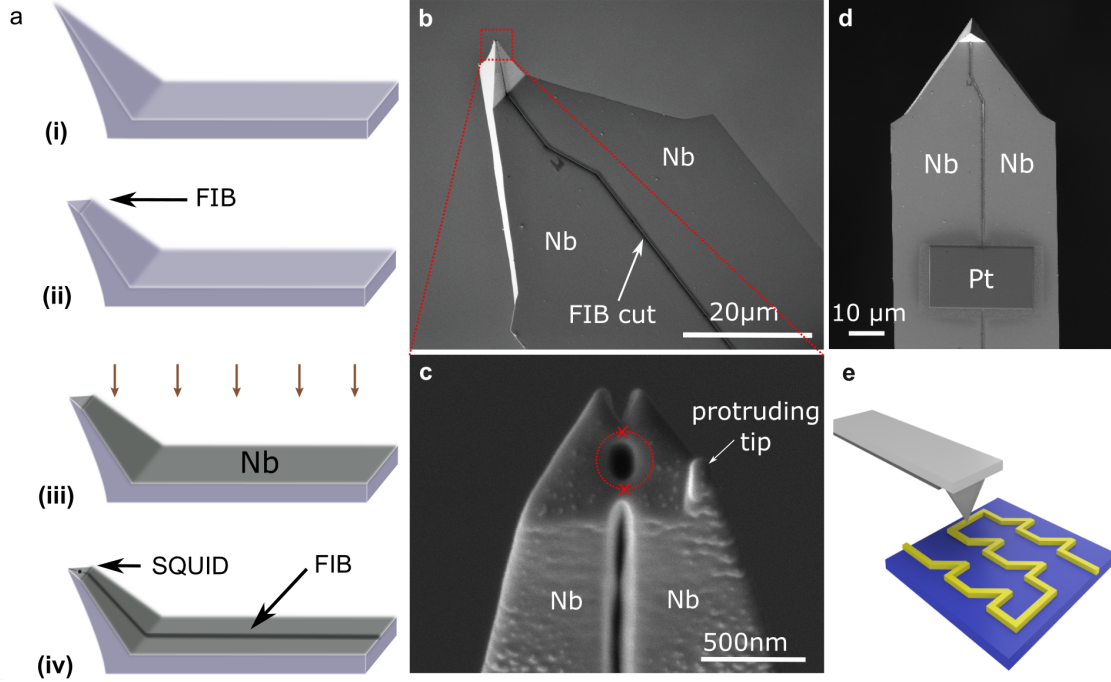


Figure 1. SQUID-on-lever fabrication. (a) Schematic of the steps for patterning a Nb SQUID-on-lever. (i) The tip of an AFM cantilever (ii) is milled away to create a triangular plateau. (iii) A Nb film is deposited on the front side of the cantilever and (iv) is then milled via FIB to define a SQUID. (b) SEM image from below the Si cantilever showing the Nb film and the FIB-milled trench separating the two leads to the on-tip device. (c) Zoomed-in SEM image showing the FIB-milled trenches and central hole defining the SQUID device. (d) Pt shunt resistance connecting two Nb leads. (e) Schematic of the scanning probe and sample.

operating under vacuum at 4.2 K. Piezoelectric positioners move the sample under the cantilever with nanometer-scale precision and a specialized cantilever holder allows for both electrical contact to the SQUID-on-lever as well as mechanical excitation. The cantilever's flexural motion is driven by a piezoelectric disc mounted next to the cantilever at its fundamental resonance frequency f_0 of around 300 kHz and is detected using a fiber-optic interferometer. As the cantilever is approached to the substrate, f_0 shifts, due to tip-sample interaction. This shift Δf is plotted as a function of tip-sample distance z in Fig. 2 (a). The inset of Fig. 2 (a) shows a significant response in Δf even for $z > 1 \mu\text{m}$. As in standard non-contact AFM, this interaction enables a controlled approach to the sample, as well as the ability to safely scan within a few tens of nanometers of the sample surface by feeding back and stabilizing at a constant Δf .

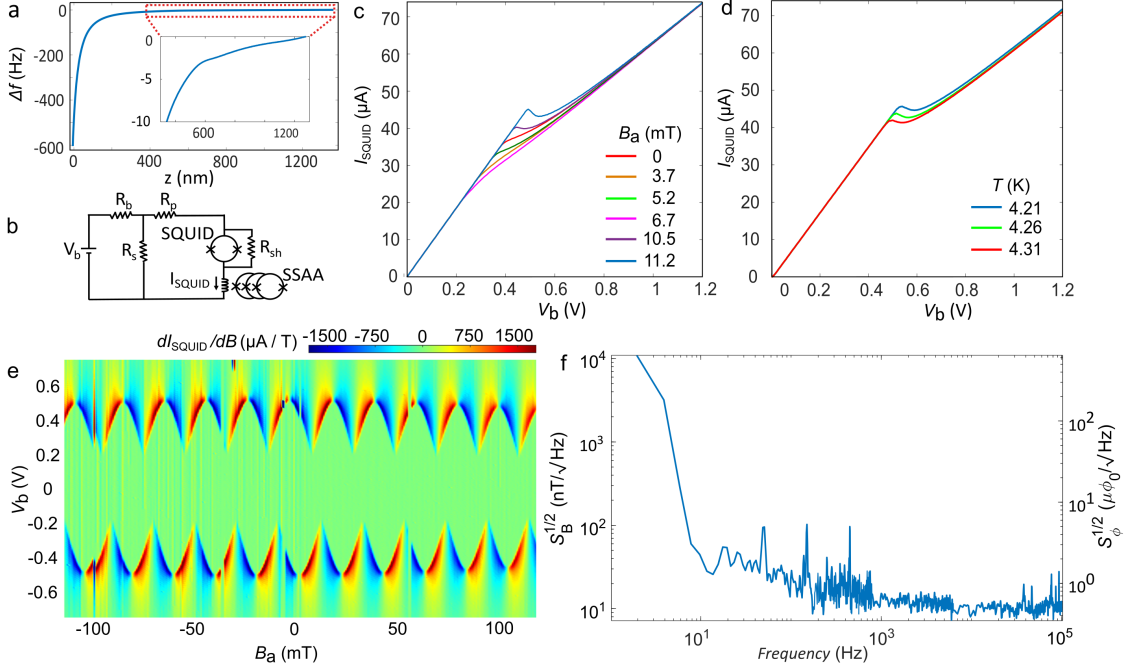


Figure 2. SQUID-on-lever characterization. (a) $\Delta f(z)$ curve showing an approach of the cantilever to the sample surface. (b) Schematic of the measurement circuit including inductive coupling to a SSAA, where $R_b = 6.1k\Omega$, $R_s = 3\Omega$, $R_p = 2\Omega$, $R_{sh} = 4\Omega$. (c) $I_{\text{SQUID}}(V_b)$ curves of the Nb SQUID-on-lever measured at 4.2 K and at different B_a applied along the axis of the SQUID. (d) $I_{\text{SQUID}}(V_b)$ curves measured at different T and $B_a = 0$. (e) Magnetic response function dI_{SQUID}/dB of the SQUID as a function of both V_b and B_a , showing the quantum interference pattern of the SQUID-on-lever. (f) Power spectral density of the device at 4.2 K, expressed both in terms of magnetic field (left axis) and flux quanta (right axis). White noise of the device reaches $0.48 \mu\Phi_0/\sqrt{\text{Hz}}$ or $9.5 \text{ nT}/\sqrt{\text{Hz}}$

We characterize the magnetic and thermal sensitivity of the SQUID-on-lever at 4.2 K using the electrical circuit in Fig. 2 (b). We operate the SQUID in unconventional voltage-bias mode with a large bias resistor, R_b and a small shunt resistor, R_s . The circuit includes a parasitic resistance R_p in series with the SQUID due to the wires and contacts. The Pt shunt resistance R_{sh} is connected in parallel with the SQUID and helps to reduce hysteresis in the SQUID's $I_{\text{SQUID}}(V_b)$ response, by damping its high frequency dynamics. We measure the current through the SQUID I_{SQUID} using a cold SQUID series array amplifier (SSAA) working in feedback mode. Figs. 2 (c) and (d) show plots of $I_{\text{SQUID}}(V_b)$ measured at different applied magnetic fields and temperatures respectively. The measurements show a maximum

critical current $I_c = 45 \mu\text{A}$ at 4.2 K. A magnetic field B_a applied along the axis of the SQUID loop \hat{z} produces a modulation of the critical current of $25 \mu\text{A}$, which persists up to 1.0 T. From measurements of $I_{\text{SQUID}}(V_b)$ at different temperatures T , shown in Fig. 2 (d), I_c is seen to decrease with increasing T .

In Fig. 2 (e), we plot the magnetic response function dI_{SQUID}/dB , where B is the total magnetic field, as a function of V_b and B_a , showing a pronounced quantum interference pattern with a period of 20 mT. This period corresponds to an effective SQUID loop diameter of 365 nm, which is slightly larger than the diameter measured in the SEM image in Fig. 1 (c). This mismatch is likely due to both magnetic field lensing by the superconductor on the triangular plateau and the suppression of superconductivity caused by ion implantation in the Nb near the milled regions. The interference pattern shows a large asymmetry between positive and negative V_b , due to the asymmetry of the two JJs. By appropriate choice of V_b , this asymmetry increases the range of applied fields, in which the SQUID is sensitive, including at $B_a = 0$.

Fig. 2 (f) shows the spectral density of the SQUID's noise both in terms of magnetic flux and magnetic field measured at $B_a = 0$ and $V_b = 0.5$ V. The spectrum is dominated by $1/f$ -like noise at low frequencies and white noise $S_{\Phi}^{1/2}$ under $1 \mu\Phi_0/\sqrt{\text{Hz}}$ above a few hundred Hz. At 10 kHz and in the sensitive regions of the magnetic response function, the magnetic field sensitivity reaches $S_B^{1/2} 9.5 \text{ nT}/\sqrt{\text{Hz}}$, which corresponds to a flux sensitivity $S_{\Phi}^{1/2}$ of $0.48 \mu\Phi_0/\sqrt{\text{Hz}}$. This sensitivity is significantly better than previously reported SQUID-on-tip sensors made from Al¹, Nb², and Mo₆₆Re₃₄¹⁵, but does not attain the sensitivity of state-of-the-art Pb SQUID-on-tips⁵.

We determine the thermal sensitivity of the device, by analyzing measurements of $I_{\text{SQUID}}(V_b)$ taken at different T , as in Fig. 2 (d). We calculate the thermal response dI_{SQUID}/dT from the slope of $I_{\text{SQUID}}(T)$ curve at a fixed bias voltage V_b . For $V_b = 0.55$ V and at $B_a = 0$ and $T = 4.2$ K, $dI_{\text{SQUID}}/dT = -24.2 \mu\text{A}/\text{K}$. This response and the corresponding white noise floor of the device yields a thermal sensitivity better than $620 \text{ nK}/\sqrt{\text{Hz}}$, which is comparable to the the state-of-the-art Pb SQUID-on-tip sensors.

In order to demonstrate the capabilities of the SQUID-on-lever as a scanning probe, we first image a current-carrying Au-wire patterned on a Si substrate. We image the topography of the wire with our SQUID-on-lever by implementing a standard non-contact AFM technique: scanning in the xy -plane while feeding back on the piezoelectric scanner controlling the

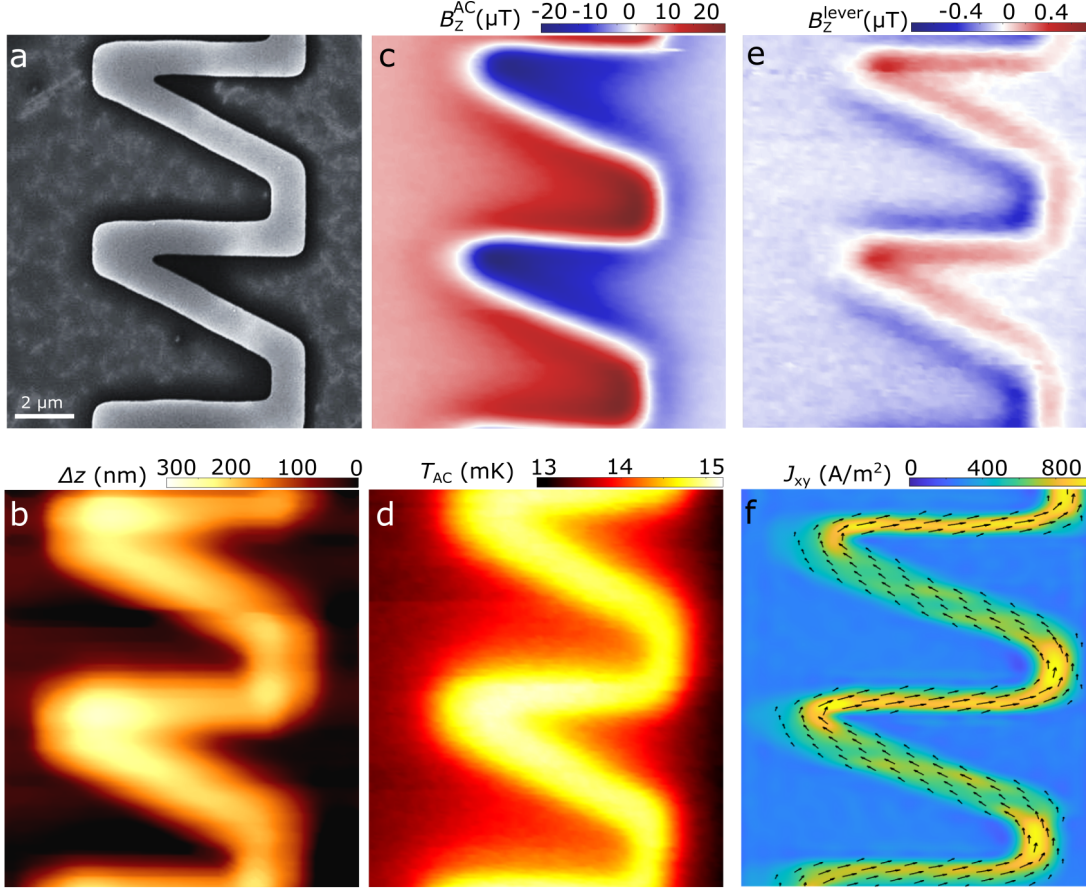


Figure 3. Scanning probe images of a current-carrying wire taken by a SQUID-on-lever. (a) SEM image of the 750-nm-wide and 300-nm-thick saw-tooth-shaped Au wire patterned on a Si substrate. (b) Non-contact AFM image taken using the SQUID-on-lever in constant-frequency mode showing the sample topography Δz taken at a tip-sample spacing $z = 140$ nm. Scanning probe images made by the SQUID-on-lever at constant height from the substrate corresponding to $z = 345$ nm of (c) the z -component of the Biot-Savart field B_z^{AC} and (d) the AC temperature modulation T_{AC} produced by $I_{\text{AC}} = 100 \mu\text{A}$ of current flowing through the wire. (e) Image of z -component of the magnetic field B_z^{lever} at the cantilever oscillation frequency produced by $I_{\text{DC}} = 200 \mu\text{A}$ of DC. This signal is proportional to the spatial derivative of B_z along the cantilever oscillation direction \hat{z} . (f) A map of the current density \mathbf{J}_{xy} flowing through the wire calculated from the measurement of B_z^{AC} in (c). The color scale indicates the magnitude and the arrows the direction of \mathbf{J}_{xy} .

the tip-sample spacing z with a correction Δz to maintain a constant frequency shift Δf (constant frequency mode). In Fig. 3 (b) we present the AFM image of the Au-wire scanned at a constant $\Delta f = -5\text{Hz}$ which corresponds to a tip-sample spacing of about $z = 140$ nm.

The low spatial resolution of the image is set by the small Δf set-point resulting in a large tip-sample spacing and wide dimension of the triangular plateau (a higher resolution topographic image is presented in Fig. 4 (a)). By measuring the SQUID response while scanning over the same area at a fixed height corresponding to $z = 345$ nm over the substrate, we image the Biot-Savart field and the thermal dissipation produced by alternating current (AC) flowing through the wire. Note that the SQUID-to-sample spacing $z_{\text{SQUID}} = z + 175$ nm, due to the height of the protruding tip. Fig. 3 (c) shows the z -component of the Biot-Savart field B_z^{AC} produced by $I_{\text{AC}} = 100 \mu\text{A}$ of current at $f_{\text{AC}} = 4.17$ kHz. Sensitivity to magnetic field is achieved by choosing a combination of B_a and V_b , in which the SQUID-on-lever has a strong magnetic response, which is plotted in Fig. 2 (d), and measuring the first harmonic response of the SQUID at f_{AC} . By introducing a few mbar of ^4He exchange-gas into the vacuum chamber, we also make our SQUID-on-lever sensitive to the local temperature modulation T_{AC} produced by Joule heating as AC flows through the Au wire. The ability to sensitively map T_{AC} is made possible by the thermal coupling of the sensor to the sample. In particular, this exchange-gas-mediated coupling must be stronger than the coupling of the sensor to its support. To be a non-invasive probe, this coupling must also be weaker than the coupling of the sample with its substrate. Both of these conditions are met in our system, where the sensor is very weakly coupled to its support, because of the small geometrical cross-section of the cantilever and the absence of thermal conductivity along the superconducting film. Because $T_{\text{AC}} \ll T$, where the bath temperature $T = 4.2$ K, T_{AC} is in the small signal limit and is proportional to the power dissipated, i.e. the square of the flowing current¹³. Therefore to image T_{AC} , we map the second harmonic response of the SQUID to the current at $2f_{\text{AC}}$ ¹³, as shown in Fig. 3 (d) with $I_{\text{AC}} = 100 \mu$.

Fig. 3 (e) shows another imaging mode available to the SQUID-on-lever probe: we actuate the cantilever's fundamental mode at $f_0 = 282$ kHz with an amplitude of 15 nm and measure the z -component of the magnetic field at this frequency B_z^{lever} . The resulting image, measured at a constant height corresponding to $z = 345$ nm over the substrate, is proportional to the spatial derivative of the magnetic field along the cantilever oscillation direction dB_z/dz produced by $I_{\text{DC}} = 200 \mu\text{A}$ of direct current (DC) flowing through the wire. The use of lock-in techniques to demodulate and spectrally filter the resulting signal substantially reduces $1/f$ -noise, which dominates DC measurements of B_z . Imaging such spatial magnetic field derivatives also increases the maximum sensitivity towards smaller features sizes,

compared with imaging magnetic fields¹⁶. In fact, detection of magnetic spatial derivatives is the standard mode for MFM and has also been implemented using a tuning fork resonator in scanning SQUID-on-tip microscopy¹², in order to increase sensitivity to small DC features in B_z or local T .

The image of the Biot-Savart field produced by current flowing through the Au wire, shown in Fig. 3 (c), can be reconstructed into a map of the current density \mathbf{J}_{xy} by inverting the Biot-Savart law^{17,18}. Although 3D current densities do not produce a unique magnetic stray field patterns and can therefore not be determined by stray magnetic field imaging alone, in-plane current densities or current densities which are uniform throughout the thickness do. By assuming a uniform \mathbf{J}_{xy} throughout the thickness of the Au wire, we reconstruct the current density shown in Fig. 3 (f).

In order to demonstrate the probe’s applicability to nanomagnetic samples, we image an artificial spin ice^{19,20}, shown in Fig. 4 (a), consisting of a lattice of lithographically patterned nanometer-scale magnets, geometrically arranged to exhibit magnetic frustration. These samples are characterized by collective excitations such as emergent magnetic monopoles^{19,21,22} or spin wave modes^{23,24}. In Fig. 4 (b), we show the sample’s topography imaged using the SQUID-on-lever as a non-contact AFM in constant-frequency mode. We use a set-point of $\Delta f = -120$ Hz, corresponding to $z = 65$ nm. The resulting image shows the array of nanomagnets with a resolution on the order of 50 nm. The brightest and highest resolution features in the image are due to the protruding tip patterned on the SQUID-on-lever, shown in Fig. 1 (c). Fainter and lower resolution ‘shadows’ correspond to the sample’s interaction with the larger and more distant plateau section of the tip, on which the SQUID is patterned.

Fig. 4 (c) shows a map taken at a constant height corresponding to $z = 275$ nm above the substrate ($z_{\text{SQUID}} = 450$ nm) over the same region the sample. We measure the SQUID response I_{SQUID} to the magnetic stray field B_z produced by the spin ice at remanence following saturation by an applied magnetic field along \hat{y} , $B_{ay} = 100$ mT. This corresponds to a two-in/two-out type-II state of the square ice. The measurement is in good agreement with the expected $B_z(x, y)$ obtained from corresponding micromagnetic simulations²⁵ which is presented in Fig. 4 (e). The position and magnetization of the simulated islands is overlaid onto this map, in order to clarify the origin of the stray field pattern. Following a minor hysteresis loop (applying a magnetic field $B_{ax} = 9.3$ mT and then reducing to zero), we

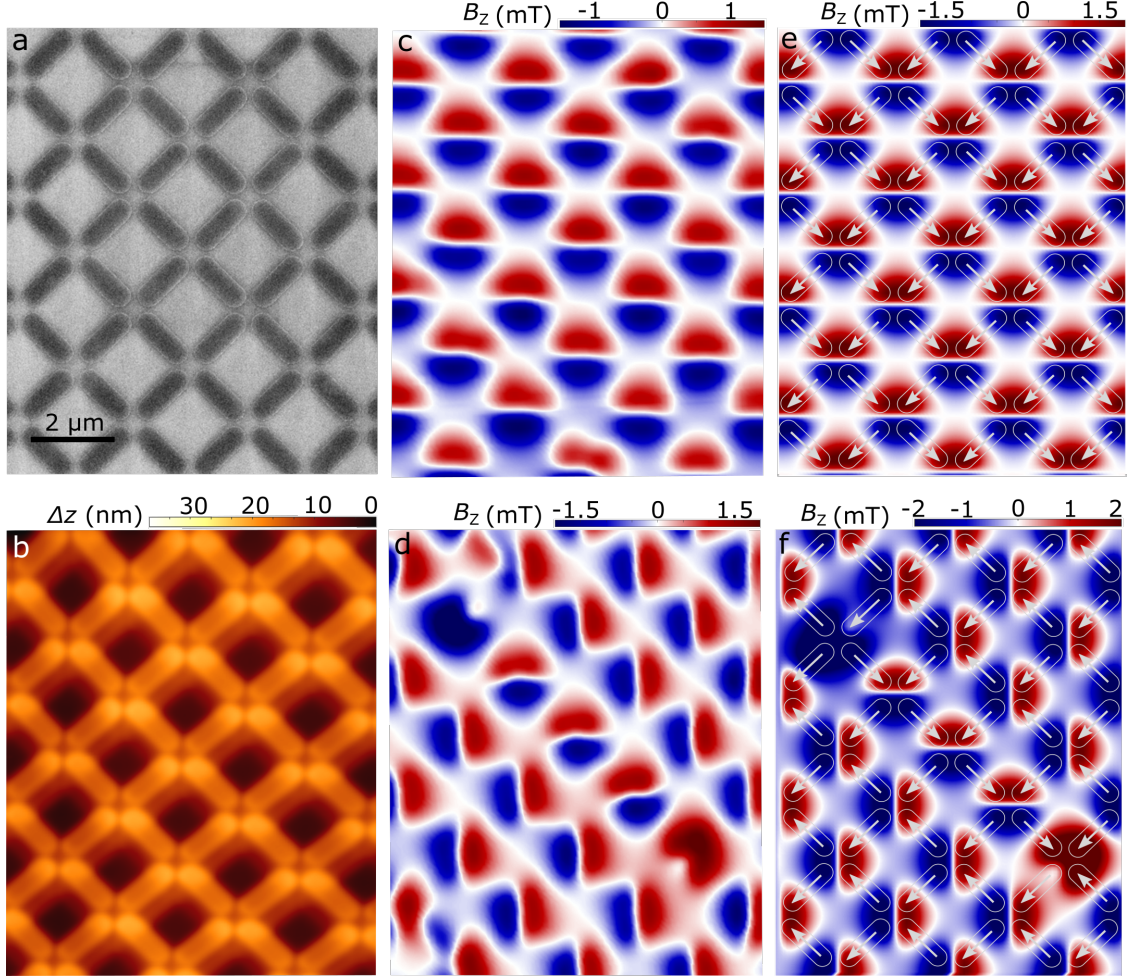


Figure 4. Scanning probe images of artificial spin ice taken by a SQUID-on-lever. (a) SEM image of the nanomagnet array consisting of a square lattice of 20-nm-thick Py islands with a lateral size of $550 \text{ nm} \times 1550 \text{ nm}$ patterned on a Si substrate. (b) Non-contact AFM image taken in constant-frequency mode showing the sample topography Δz at a tip-sample spacing $z = 65 \text{ nm}$. (c) Magnetic stray field along the z -direction B_z measured by the scanning SQUID-on-lever at constant height corresponding to $z = 275 \text{ nm}$ from the substrate. The spin ice is in remanence after saturation along \hat{y} and (d) after the execution of a minor hysteresis loop, showing the signatures of separated magnetic charges and their corresponding numerical simulations in (e) and (f). The position of the nanomagnets is shown schematically and arrows show the orientation of their magnetic moment.

record another image of the same region, shown in Fig. 4 (d). Whereas magnetic charges are compensated at each four-nanomagnet vertex in the type-II configuration (Figs. 4 (c)

and (e)), after the minor loop, two particular vertices are left with uncompensated charges (Fig. 4 (d)). A string of vertices with compensated charges, whose distribution is rotated with respect to the rest of the array, connect these poles. Fig. 4 (f) shows the results of corresponding micromagnetic simulations matching the measurements. The orientation of each nanomagnet’s magnetic moment, reveals that the poles correspond to ‘monopoles’ or type-III vertices. The asymmetric distribution of the stray fields around these points is due to the three-in/one-out or one-in/three-out configuration of the vertices.

Previous attempts at realizing on-tip SQUIDs have all involved either micrometer-sized sensors and/or coupling to stiff tuning fork resonators, which preclude topographic contrast or tip-sample stabilization for spacings larger than tens of nanometers^{2,26,27}. The principle obstacle to realizing a nanometer-scale SQUID-on-lever has been the difficulty of patterning a tiny superconducting circuit on a high-aspect-ratio tip. Our work shows that FIB patterning – with its ability to mill superconducting materials on the nanometer-scale and on non-planar surfaces – provides a solution to this technical challenge. In addition, it may be possible to pattern even smaller SQUID-on-lever devices via focused ion beam or focused electron beam induced deposition of superconducting nanostructures, e.g. from WC²⁸, or via the structural modification of superconductors via a He⁺ FIB, e.g. as demonstrated in YBCO²⁹. Moreover, more complex SQUID devices that those demonstrated here, including modulation lines or coils for susceptibility measurements, could also be patterned using FIB milling. Such increased device complexity could significantly expand the capabilities of scanning probe microscopy, which – although spectacularly successful – is typically carried out with simple probes, such as sharp conducting, insulating, or magnetic tips.

METHODS

SQUID-on-lever fabrication. The non-contact AFM cantilever (Nanosensors ATEC-NC) used here is made from doped single-crystal Si and has a fundamental mechanical resonance frequency $f_0 = 335$ kHz, spring constant $k = 45$ N/m, length $l = 160$ μm , widths $w = 45$ μm , and thickness $t = 4.6$ μm . We deposit 5 nm of Ti, 50 nm of Nb, and 2 nm of Pt on the front-side of the cantilever via sputtering deposition. Ti and Pt are used as sticking and protection layers, respectively. Prior to sputtering, the chamber is pumped to a pressure of 5×10^{-10} mbar. 200 W of DC power are used during sputtering with a flow of 40 sccm

of Ar gas and a pressure of 4 mbar. After sputtering, we evaporate a 10-nm-thick layer of Au to reduce ion implantation in subsequent FIB-milling steps. FIB-milling is done in a dual-beam SEM and FIB (FEI Helios Nano Lab 650) in a pressure of 1×10^{-5} mbar. Milling of the cantilever tip into a triangular plateau is done with a beam current of 1.1 pA. Milling of the trenches is carried out in 5 steps with different currents optimized to protect the Nb from ion implantation. For the long trench, far from the device area, a beam voltage of 30 kV and beam current of 0.4 nA is used. Closer to the final device, the beam current is reduced in steps down to 1.1 pA at the plateau. The rectangular Pt shunt resistance, shown in Fig. 1 (d), measures $30 \times 20\text{-}\mu\text{m}^2$, is 20-nm-thick, and is patterned via FIB-induced deposition using a voltage of 30 kV and beam current of 80 pA.

Sample fabrication. The current-carrying Au wire is patterned on a Si substrate using e-beam lithography and deposited via e-beam deposition. The artificial spin ice, consisting of an array of permalloy ($\text{Ni}_{83}\text{Fe}_{17}$) nanomagnets in a square ice geometry, were fabricated on a non-magnetic Si (100) substrate via electron-beam lithography, thermal evaporation at room temperature under a pressure of 10^{-6} mbar, and lift-off. The nanomagnets are $1.55\ \mu\text{m}$ -long, 560 nm-wide, and have a lattice constant of $1.5\ \mu\text{m}$. A 2-nm-thick Al capping layer is evaporated on top of the permalloy to prevent oxidation. The thickness of the nanomagnets is measured by AFM to be 10 nm on average across the entire array, without taking the capping layer into account. The thickness is chosen to ensure that the nanomagnets are in a single-domain state¹¹.

Scanning probe microscopy. The scanning probe microscope operates under high vacuum in a ^4He cryostat and employs piezoelectric walkers and scanners (Attocube ANPx311/LT/HV, ANSxy100lr/LT/HV) to move the sample. The fiber-optic interferometer consists of a 1550-nm diode laser, a 95:5 fiber-optic coupler, a fast and a custom-built objective focusing light onto the cantilever to an $8\ \mu\text{m}$ spot. The resulting low-finesse Fabry-Perot interferometer acts as a sensitive sensor of the cantilever's flexural motion, where the interference intensity is measured by a fast photo-receiver with an effective 3-dB-bandwidth of 800 kHz. The cavity is stabilized against drift using a PID loop (Zurich Instruments MFLI) controlling the laser temperature. The incident power of around $1\ \mu\text{W}$ does not significantly heat the cantilever, as confirmed by measurements of laser power dependence and mechanical thermal motion. During approach and scanning a phase-locked loop (Zurich Instruments MFLI) is used to excite and determine cantilever's mechanical resonance frequency f_0 . f_0 .

Current reconstruction and micromagnetic simulations. Reconstruction of the current flowing through the Au wire is carried out using the $B_z(x, y)$ measurements and following the procedures in refs.^{17,18}. Micromagnetic simulations are performed with the *Mumax* software package³⁰, which employs the Landau-Lifshitz-Gilbert micromagnetic formalism using finite-difference discretization. The size, shape, and material parameters of the simulated nanomagnets correspond to those of the measured spin ice sample. We use typical parameters for permalloy: saturation magnetization $\mu_0 M_S = 1$ T, exchange constant $A_{ex} = 1.3 \times 10^{-11}$ J/m, and no magnetocrystalline anisotropy, $K = 0$. A temperature $T = 0$ is assumed. The structure is discretized into cells of size $9.19 \text{ nm} \times 9.19 \text{ nm} \times 10 \text{ nm}$.

AUTHOR CONTRIBUTIONS

M.P and M.W. conceived and designed the experiment. M.W., D.J. and K.B. fabricated the SQUID-on-lever. K.B. and D.J. performed the characterization measurements with help from M.W and E.M. The scanning probe measurements were carried out by K.B., M.W., D.J., and A.V. D.J., B.G., and S.G. performed micromagnetic simulations. J.R. and C.S. provided the Nb sputtering system. S.G. fabricated the nanomagnet arrays. M.P. wrote the manuscript with input from K.B. and M.W. All authors discussed the results and commented on the manuscript. M.P. supervised the project. The authors declare that they have no competing financial interests.

ACKNOWLEDGMENTS

We thank Roy Haller for contributions to the sputtering high-quality Nb and José María De Teresa for important suggestions. We also thank Sascha Martin and his team in the machine shop of the Physics Department at the University of Basel for help building the measurement system. We acknowledge the European Commission under H2020 FET Open grant ‘FIBsuperProbes’ (number 892427), H2020 ERC Advanced grant TopSupra, the SNF under Grant 200020-178863, the Swiss Nanoscience Institute, the Kanton Aargau, and the

- ¹ Amit Finkler, Yehonathan Segev, Yuri Myasoedov, Michael L. Rappaport, Lior Ne'eman, Denis Vasyukov, Eli Zeldov, Martin E. Huber, Jens Martin, and Amir Yacoby. Self-Aligned Nanoscale SQUID on a Tip. *Nano Lett.*, 10(3):1046–1049, March 2010.
- ² A. Finkler, D. Vasyukov, Y. Segev, L. Ne'eman, E. O. Lachman, M. L. Rappaport, Y. Myasoedov, E. Zeldov, and M. E. Huber. Scanning superconducting quantum interference device on a tip for magnetic imaging of nanoscale phenomena. *Review of Scientific Instruments*, 83(7):073702, July 2012.
- ³ A. Uri, S. Grover, Y. Cao, J. A. Crosse, K. Bagani, D. Rodan-Legrain, Y. Myasoedov, K. Watanabe, T. Taniguchi, P. Moon, M. Koshino, P. Jarillo-Herrero, and E. Zeldov. Mapping the twist-angle disorder and Landau levels in magic-angle graphene. *Nature*, 581(7806):47–52, May 2020. Number: 7806 Publisher: Nature Publishing Group.
- ⁴ C. L. Tschirhart, M. Serlin, H. Polshyn, A. Shragai, Z. Xia, J. Zhu, Y. Zhang, K. Watanabe, T. Taniguchi, M. E. Huber, and A. F. Young. Imaging orbital ferromagnetism in a moiré Chern insulator. *Science*, 372(6548):1323–1327, June 2021. Publisher: American Association for the Advancement of Science Section: Report.
- ⁵ Denis Vasyukov, Yonathan Anahory, Lior Embon, Dorri Halbertal, Jo Cuppens, Lior Neeman, Amit Finkler, Yehonathan Segev, Yuri Myasoedov, Michael L. Rappaport, Martin E. Huber, and Eli Zeldov. A scanning superconducting quantum interference device with single electron spin sensitivity. *Nat Nano*, 8(9):639–644, September 2013. tex.ids: vasyukov_scanning_2013-1.
- ⁶ L. Embon, Y. Anahory, A. Suhov, D. Halbertal, J. Cuppens, A. Yakovenko, A. Uri, Y. Myasoedov, M. L. Rappaport, M. E. Huber, A. Gurevich, and E. Zeldov. Probing dynamics and pinning of single vortices in superconductors at nanometer scales. *Scientific Reports*, 5:7598, January 2015.
- ⁷ L. Ceccarelli, D. Vasyukov, M. Wyss, G. Romagnoli, N. Rossi, L. Moser, and M. Poggio. Imaging pinning and expulsion of individual superconducting vortices in amorphous MoSi thin films. *Phys. Rev. B*, 100(10):104504, September 2019.
- ⁸ Ella O. Lachman, Andrea F. Young, Anthony Richardella, Jo Cuppens, H. R. Naren, Yonathan Anahory, Alexander Y. Meltzer, Abhinav Kandala, Susan Kempinger, Yuri Myasoedov, Mar-

- tin E. Huber, Nitin Samarth, and Eli Zeldov. Visualization of superparamagnetic dynamics in magnetic topological insulators. *Science Advances*, 1(10):e1500740, November 2015.
- ⁹ Y. Anahory, L. Embon, C. J. Li, S. Banerjee, A. Meltzer, H. R. Naren, A. Yakovenko, J. Cuppens, Y. Myasoedov, M. L. Rappaport, M. E. Huber, K. Michaeli, T. Venkatesan, Ariando, and E. Zeldov. Emergent nanoscale superparamagnetism at oxide interfaces. *Nature Communications*, 7:12566, August 2016.
- ¹⁰ D. Vasyukov, L. Ceccarelli, M. Wyss, B. Gross, A. Schwarb, A. Mehlin, N. Rossi, G. Tütüncüoğlu, F. Heimbach, R. R. Zamani, A. Kovács, A. Fontcuberta i Morral, D. Grundler, and M. Poggio. Imaging Stray Magnetic Field of Individual Ferromagnetic Nanotubes. *Nano Lett.*, 18(2):964–970, February 2018.
- ¹¹ Marcus Wyss, Sebastian Gliga, Denis Vasyukov, Lorenzo Ceccarelli, Giulio Romagnoli, Jizhai Cui, Armin Kleibert, Robert L. Stamps, and Martino Poggio. Stray-Field Imaging of a Chiral Artificial Spin Ice during Magnetization Reversal. *ACS Nano*, December 2019.
- ¹² Aviram Uri, Youngwook Kim, Kousik Bagani, Cyprian K. Lewandowski, Sameer Grover, Nadav Auerbach, Ella O. Lachman, Yuri Myasoedov, Takashi Taniguchi, Kenji Watanabe, Jurgen Smet, and Eli Zeldov. Nanoscale imaging of equilibrium quantum Hall edge currents and of the magnetic monopole response in graphene. *Nature Physics*, 16(2):164–170, February 2020. Number: 2 Publisher: Nature Publishing Group.
- ¹³ D. Halbertal, J. Cuppens, M. Ben Shalom, L. Embon, N. Shadmi, Y. Anahory, H. R. Naren, J. Sarkar, A. Uri, Y. Ronen, Y. Myasoedov, L. S. Levitov, E. Joselevich, A. K. Geim, and E. Zeldov. Nanoscale thermal imaging of dissipation in quantum systems. *Nature*, 539(7629):407–410, November 2016.
- ¹⁴ Dorri Halbertal, Moshe Ben Shalom, Aviram Uri, Kousik Bagani, Alexander Y. Meltzer, Ido Marcus, Yuri Myasoedov, John Birkbeck, Leonid S. Levitov, Andre K. Geim, and Eli Zeldov. Imaging resonant dissipation from individual atomic defects in graphene. *Science*, 358(6368):1303–1306, December 2017.
- ¹⁵ Kousik Bagani, Jayanta Sarkar, Aviram Uri, Michael L. Rappaport, Martin E. Huber, Eli Zeldov, and Yuri Myasoedov. Sputtered Mo₆₆Re₃₄ SQUID-on-Tip for High-Field Magnetic and Thermal Nanoimaging. *Phys. Rev. Applied*, 12(4):044062, October 2019. Publisher: American Physical Society.

- ¹⁶ Estefani Marchiori, Lorenzo Ceccarelli, Nicola Rossi, Luca Lorenzelli, Christian L. Degen, and Martino Poggio. Technical Review: Imaging weak magnetic field patterns on the nanometer-scale and its application to 2D materials. *arXiv:2103.10382 [cond-mat, physics:quant-ph]*, March 2021. arXiv: 2103.10382.
- ¹⁷ Bradley J. Roth, Nestor G. Sepulveda, and John P. Wikswo. Using a magnetometer to image a two-dimensional current distribution. *Journal of Applied Physics*, 65(1):361–372, January 1989.
- ¹⁸ K. Chang, A. Eichler, J. Rhensius, L. Lorenzelli, and C. L. Degen. Nanoscale Imaging of Current Density with a Single-Spin Magnetometer. *Nano Lett.*, 17(4):2367–2373, April 2017.
- ¹⁹ R. F. Wang, C. Nisoli, R. S. Freitas, J. Li, W. McConville, B. J. Cooley, M. S. Lund, N. Samarth, C. Leighton, V. H. Crespi, and P. Schiffer. Artificial ‘spin ice’ in a geometrically frustrated lattice of nanoscale ferromagnetic islands. *Nature*, 439(7074):303–306, January 2006.
- ²⁰ Sandra H. Skjærvø, Christopher H. Marrows, Robert L. Stamps, and Laura J. Heyderman. Advances in artificial spin ice. *Nature Reviews Physics*, 2(1):13–28, January 2020.
- ²¹ Elena Mengotti, Laura J. Heyderman, Arantxa Fraile Rodriguez, Frithjof Nolting, Remo V. Hugli, and Hans-Benjamin Braun. Real-space observation of emergent magnetic monopoles and associated Dirac strings in artificial kagome spin ice. *Nat Phys*, 7(1):68–74, January 2011.
- ²² Alan Farhan, Michael Saccone, Charlotte F. Petersen, Scott Dhuey, Rajesh V. Chopdekar, Yen-Lin Huang, Noah Kent, Zuhuang Chen, Mikko J. Alava, Thomas Lippert, Andreas Scholl, and Sebastiaan van Dijken. Emergent magnetic monopole dynamics in macroscopically degenerate artificial spin ice. *Science Advances*, 5(2), 2019.
- ²³ Ezio Iacocca, Sebastian Gliga, Robert L. Stamps, and Olle Heinonen. Reconfigurable wave band structure of an artificial square ice. *Phys. Rev. B*, 93(13):134420, April 2016.
- ²⁴ Ezio Iacocca and Olle Heinonen. Topologically Nontrivial Magnon Bands in Artificial Square Spin Ices with Dzyaloshinskii-Moriya Interaction. *Phys. Rev. Applied*, 8(3):034015, September 2017.
- ²⁵ Attila Kakay, Elmar Westphal, and Riccardo Hertel. Speedup of FEM Micromagnetic Simulations With Graphical Processing Units. *IEEE Transactions on Magnetics*, 46(6):2303–2306, June 2010. Conference Name: IEEE Transactions on Magnetics.
- ²⁶ Yusuke Shibata, Shintaro Nomura, Hiromi Kashiwaya, Satoshi Kashiwaya, Ryosuke Ishiguro, and Hideaki Takayanagi. Imaging of current density distributions with a Nb weak-link scanning nano-SQUID microscope. *Scientific Reports*, 5:15097, October 2015.

- ²⁷ John R. Kirtley, Lisa Paulius, Aaron J. Rosenberg, Johanna C. Palmstrom, Connor M. Holland, Eric M. Spanton, Daniel Schiessl, Colin L. Jermain, Jonathan Gibbons, Y.-K.-K. Fung, Martin E. Huber, Daniel C. Ralph, Mark B. Ketchen, Gerald W. Gibson, and Kathryn A. Moler. Scanning SQUID susceptometers with sub-micron spatial resolution. *Review of Scientific Instruments*, 87(9):093702, September 2016.
- ²⁸ R. Córdoba, T. I. Baturina, J. Sesé, A. Yu Mironov, J. M. De Teresa, M. R. Ibarra, D. A. Nasimov, A. K. Gutakovskii, A. V. Latyshev, I. Guillamón, H. Suderow, S. Vieira, M. R. Baklanov, J. J. Palacios, and V. M. Vinokur. Magnetic field-induced dissipation-free state in superconducting nanostructures. *Nature Communications*, 4:ncomms2437, February 2013.
- ²⁹ B. Müller, M. Karrer, F. Limberger, M. Becker, B. Schröppel, C.J. Burkhardt, R. Kleiner, E. Goldobin, and D. Koelle. Josephson Junctions and SQUIDs Created by Focused Helium-Ion-Beam Irradiation of $\text{YBa}_2\text{Cu}_3\text{O}_7$. *Phys. Rev. Applied*, 11(4):044082, April 2019. tex.ids: muller_josephson_2019-1 publisher: American Physical Society.
- ³⁰ Arne Vansteenkiste, Jonathan Leliaert, Mykola Dvornik, Mathias Helsen, Felipe Garcia-Sanchez, and Bartel Van Waeyenberge. The design and verification of Mumax3. *AIP Advances*, 4(10):107133, 2014.

Supplementary Information:

Magnetic, thermal, and topographic imaging with a nanometer-scale SQUID-on-cantilever scanning probe

M. Wyss,^{1,2} K. Bagani,¹ D. Jetter,¹ E. Marchiori,¹ A. Vervelaki,¹
B. Gross,¹ J. Ridderbos,¹ S. Gliga,³ C. Schönenberger,^{1,2} and M. Poggio^{1,2}

¹*Department of Physics, University of Basel, 4056 Basel, Switzerland*

²*Swiss Nanoscience Institute, University of Basel, 4056 Basel, Switzerland*

³*Swiss Light Source, Paul Scherrer Institute, 5232 Villigen, Switzerland*

(Dated: September 15, 2021)

S1. MODULATION OF SQUID CRITICAL CURRENT WITH FIELD

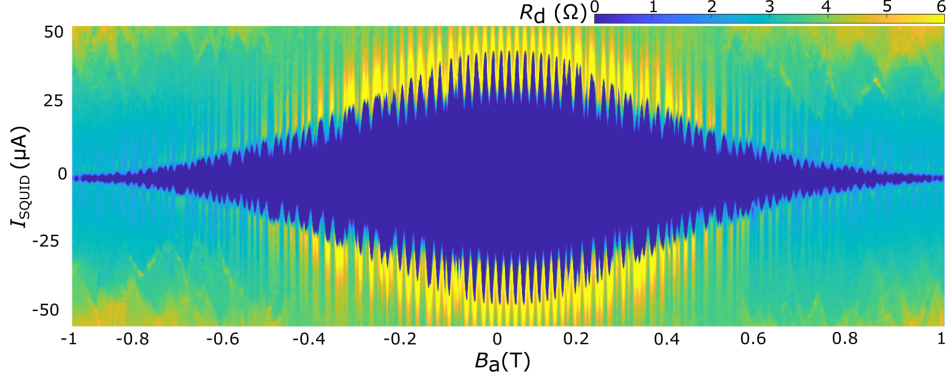


Figure S1. Differential resistance $R_d = dV_{SQUID}/dI_{SQUID}$ as a function of B_a and I_{SQUID} of the device showing SQUID interference pattern up to 1T.

Fig. S1 shows the differential resistance of the SQUID $R_d = dV_{SQUID}/dI_{SQUID}$ as a function of B_a and I_{SQUID} obtained from the measured I_{SQUID} vs. V_b curves. The SQUID shows quantum interference pattern up to $B_a = 1$ T. The interference pattern has a period of 20 mT, which translates to an effective SQUID loop diameter of 365 nm. The effective SQUID loop diameter is derived from $D = 2\sqrt{\Phi_0/\pi\Delta B}$, where Φ_0 is the flux quantum and ΔB is the period of the interference pattern.

S2. FIELD DEPENDENCE OF MAGNETIC SENSITIVITY

The magnetic sensitivity of the device is obtained from the magnetic response function dI_{SQUID}/dB and the white noise floor of the device. The magnetic response is derived from $I_{SQUID}(V_b)$ curve measured at different applied magnetic fields B_a . Fig. S2 (a) shows the plot of magnetic response with the applied magnetic field at a fixed bias $V_b = 0.4$ V. At this constant bias voltage, the spectral density of the current noise $S_I^{1/2}$ at 10 kHz is measured for the same range of B_a , as shown in Fig S2 (b). The magnetic field noise of the device is then given by $S_B^{1/2} = S_I^{1/2}/|dI_{SQUID}/dB|$. The corresponding flux noise is obtained from $S_\Phi^{1/2} = S_B^{1/2} \times (A/\Phi_0)$, where Φ_0 is the flux quantum and A is the effective area of the SQUID loop. The field noise and the flux noise of the device as a function of B_a are shown in Figs. S2 (c) and (d), respectively. The flux and field noise decrease in the high magnetic

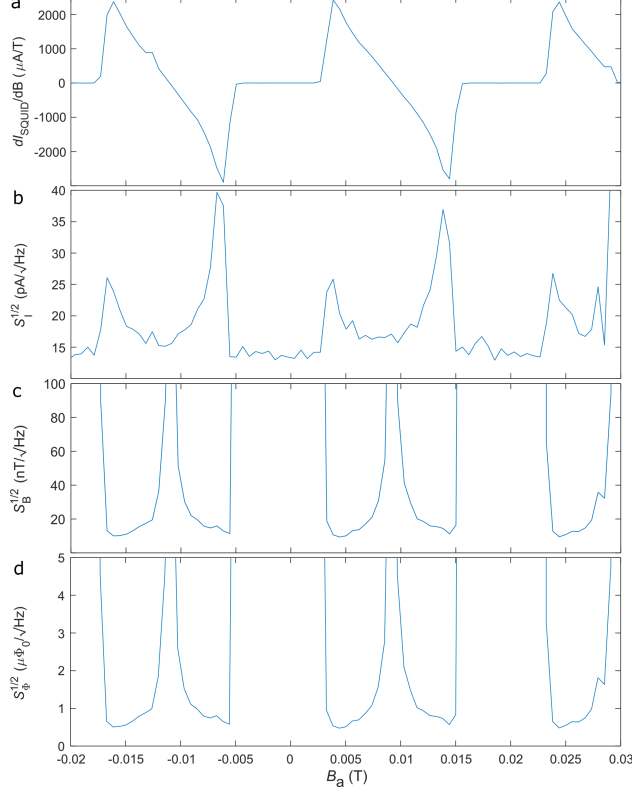


Figure S2. (a) and (b) Magnetic response function dI_{SQUID}/dB and current noise $S_I^{1/2}$ at a constant bias voltage $V_b = 0.4$ V plotted as a function of applied magnetic field B_a . (c) and (d) Corresponding field noise and flux noise of the SQUID-on-lever as a function of B_a .

response regions of the interference pattern. In the sensitive regions, the device attains a field sensitivity $S_B^{1/2} = 9.5$ nT/ $\sqrt{\text{Hz}}$ or flux sensitivity $S_\Phi^{1/2} = 0.48$ $\mu\Phi_0/\sqrt{\text{Hz}}$.

S3. THERMAL RESPONSE

In order to determine thermal sensitivity of the device, we fix the voltage bias to make the SQUID-on-lever maximally sensitive to changes in temperature. As shown in Fig. 2 (d) of the main text, where $I_{SQUID}(V_b)$ is measured at $B_a = 0$ and different T , this occurs for $V_b = 0.55$ V. At this bias voltage, we plot $I_{SQUID}(T)$ in Fig. S3. The slope of this curve yields the thermal response of the device $dI_{SQUID}/dT = -24.2$ $\mu\text{A}/\text{K}$ at 4.2 K. By measuring the white current noise $S_I^{1/2}$, we determine the temperature noise $S_T^{1/2} = S_I^{1/2}/|dI_{SQUID}/dT|$ of the device. The SQUID-on-lever reaches a thermal sensitivity $S_T^{1/2} = 620$ nK/ $\sqrt{\text{Hz}}$ at zero magnetic field and 4.2 K.

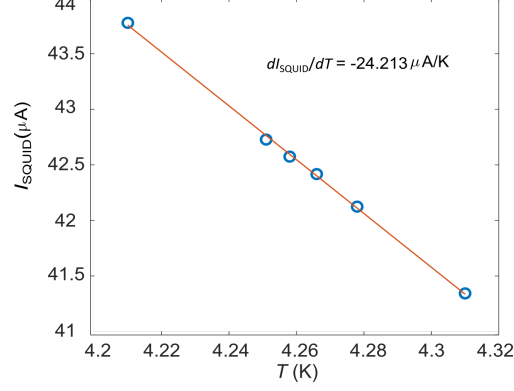


Figure S3. I_{SQUID} vs. temperature T at $V_b = 0.55$ V. Thermal response of -24.21 $\mu\text{A}/\text{K}$ is obtained from the slope.

S4. SCANNING MAGNETIC IMAGING OF THE CURRENT-CARRYING WIRE

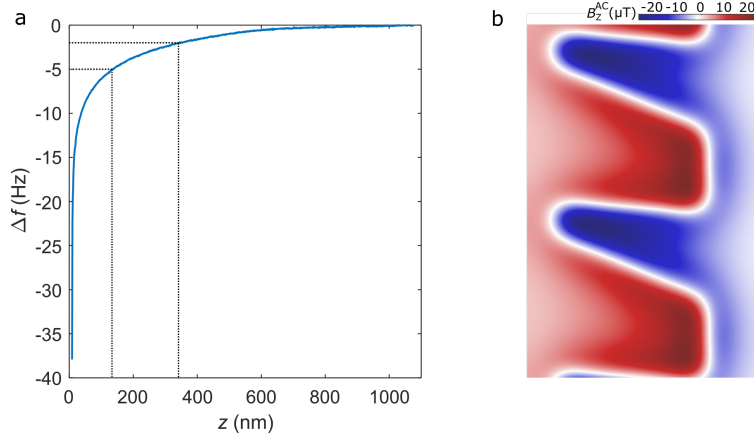


Figure S4. (a) Approach curve showing frequency shift Δf as a function of tip-sample spacing z . Dotted lines indicate the scanning height for the images of the current-carrying wire (Fig. 3 in the main text; $\Delta f = -5$ Hz) and images of the artificial spin ice (Fig. 4 in the main text; $\Delta f = -2$ Hz). (b) Simulation of the Biot-Savart field produced by the current-carrying wire at a SQUID-sample height of 520 nm.

A. Non-contact AFM

Fig. S4 (a) shows an approach curve, i.e. a measurement of the cantilever frequency shift Δf as a function of the tip-sample spacing z . The sample being approached is the current-

carrying wire imaged in Fig. 2 of the main text. The non-contact AFM image shown in Fig. 3 (b) of the main text is carried out at a set-point $\Delta f = -5$ Hz, which corresponds to a tip-sample spacing $z = 140$ nm and a SQUID-sample spacing $z_{\text{SQUID}} = 315$ nm (the height of the protruding tip is 175 nm). The large tip-sample spacing and the sample’s interaction with the large plateau at the apex of the cantilever yield the low spatial resolution apparent in the AFM of Fig. 3 (b) of the main text. As we approach closer to the sample, however, the interaction of the small protruding tip dominates over that with the plateau. As a result, the non-contact AFM shown in Fig. 4 (b) of the main text, which was taken at a tip-sample spacing of $z = 65$ nm, is characterized by a resolution on the order of 50 nm. A lower resolution ‘shadow’ is visible in the image, due to the contribution from the sample’s interaction with the large triangular plateau behind the protruding tip.

B. Simulation of Biot-Savart field

We simulate the Biot-Savart field produced by the current-carrying wire. We use COMSOL Multiphysics 5.5 AC/DC module to simulate the current density distribution inside the gold wire originating from an applied current of $100 \mu\text{A}$. The wire geometry matches the size of the measured sample and we apply typical parameters for Au at $T = 4.2$ K. We then calculate the Biot-Savart field produced by the current density and extract the z -component of the magnetic field B_z^{ac} . For these simulations we use a custom tetrahedral mesh with a minimum element size 80 nm. We filter the simulated magnetic field at a SQUID-sample distance of 520 nm with a Gaussian with standard deviation $\sigma = 365$ nm to account for the effective diameter of the SQUID loop. In Fig. S4 (b), we show the simulation of B_z^{ac} at the SQUID-sample spacing of the measurement. This simulation matches the measurement shown in Fig. 3 (c) of the main text, confirming the scanning height obtained from the approach curve shown in Fig. S4 (a).

S5. MAPPING dB_z/dz OF THE NANOMAGNET ARRAY

The SQUID-on-cantilever is actuated at its fundamental mode ($f_0 = 282$ kHz) with an amplitude of 15 nm. By measuring the magnetic field response of the SQUID at f_0 , we obtain the spatial derivative of the magnetic field along the cantilever oscillation direction

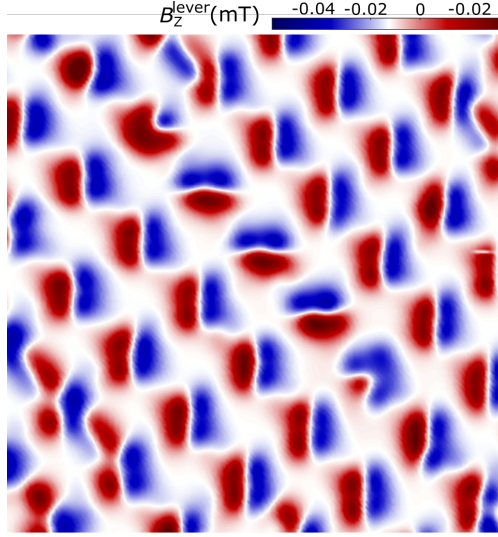


Figure S5. Image of z -component of the magnetic field B_z^{lever} at the cantilever oscillation frequency produced the artificial spin-ice sample. This signal is proportional to the spatial derivative of B_z along the cantilever oscillation direction \hat{z} . This image is analogous to that shown for the current-carrying wire in Fig. 3 (e) of the main text.

dB_z/dz . Imaging dB_z/dz increases the sensitivity and spatial resolution of the image compared to imaging magnetic fields. Fig. S5 presents dB_z/dz measured above the square lattice of nanomagnets in the type-II configuration with two type-III vertices or monopoles.